Turbulent flow in a ribbed channel: Flow structures in the vicinity of a rib

Wang, Lei; Salewski, Mirko; Sundén, Bengt

Published in:
Experimental Thermal and Fluid Science

Link to article, DOI:
10.1016/j.expthermflusci.2009.10.005

Publication date:
2010

Turbulent flow in a ribbed channel: Flow structures in the vicinity of a rib

Lei Wang[a], Mirko Salewski[b], Bengt Sundén[a]

[a] *Heat Transfer Division, Lund University, Box 118, SE-22100 Lund, Sweden*
[b] *Risø National Laboratory for Sustainable Energy, Technical University of Denmark, DK-4000 Roskilde, Denmark*

Abstract

PIV measurements are performed in a channel with periodic ribs on one wall. The emphasis of this study is to investigate the flow structures in the vicinity of a rib in terms of mean velocities, Reynolds stresses, probability density functions (PDF), and two-point correlations. The PDF distribution of u' is bimodal in the separated shear layer downstream of the rib. The maximum Reynolds shear stresses occur at the leading edge of the rib. Based on quadrant analysis, it is found that ejection motions make a dominant contribution to the Reynolds shear stress in this region. Moreover, topology-based visualization is applied to the separation bubble upstream of the rib. Salient critical points and limit cycles are extracted, which gives clues to the physical processes occurring in the flow.

Keywords: Ribbed channel, PIV, Flow separation, Topology

1. Introduction

Channels roughened with periodic ribs are widely applied in enhancing heat transfer in various cooling passages, e.g. gas turbine blades. The flow past a rib is typically characterized by flow separation and reattachment which essentially break up the viscous sub-layer and enhance the heat transfer. It is found that the heat transfer rates attain a maximum near the time-mean reattachment line [1]. Unlike the flow over a backward-facing step, the flow past a rib is more complicated since it has separation regions upstream and downstream of the obstacle, which constitutes an 'overwhelming perturbation' to the flow [2]. Even though numerous studies have been carried out to study the thermal and flow characteristics in ribbed channels, the understanding of this phenomenon is not complete. In direct numerical simulations (DNS) of turbulent channel flow with square ribs on one wall, Leonardi et al. [3] showed that main flow features, such as the size and strength of the recirculation zones, do not change significantly and reoccur along the channel as the cavity width to roughness height ratio is greater than 7. Using liquid crystals, Rau et al. [4] found a second maximum of heat transfer rate as the rib pitch ratio is greater than 10. The distance of this maximum from the rib corresponds to the extension of the separation region upstream of the obstacle. Mullin and Martin [5] investigated the turbulent flow structure over a rib-roughened surface by laser Doppler velocimetry (LDV). The main finding was that a small recirculation bubble forms along the leading edge of each rib and subsequently collapses at irregular intervals. Wang et al. [6] carried out particle image velocimetry (PIV) measurements in a ribbed channel. With aid of a Galilean decomposition scheme, they revealed distinct vortices embedded in the separated shear layer. Martinuzzi and Tropea [7] applied a crystal violet technique to study the flow field on the front face of a rib in a channel. The flow is characterized by the appearance of a nearly equally spaced array of alternating saddle and node points. Based on this observation, they conjectured a cellular structure as flow passes over an obstacle. Recently, Chou and Chao [8] performed flow visualizations to investigate the flow structures around rectangular obstacles. In their study, the U-vortices and a series of branching points were well in line with the flow model proposed by Martinuzzi and Tropea [7]. Considering the large difference in the Reynolds number between [7] and [8], the agreement is rather interesting.

Although there is difficulty in conceptually visualizing complex flow patterns, it can be facilitated by using critical-point theory. Critical points are points in the flow field where the velocity is zero and the streamline slope is indeterminate. Critical-point theory was initially developed to study the flow features in the vicinity of separation points. Depending on whether streamlines are attracted to or emanate from critical points, critical points are classified into stable and unstable types. A detailed description of critical-point theory can be found in [9]. In addition, another important topological feature is the so-called bifurcation line towards which other trajectories converge asymptotically. Bifurcation lines may be either open or closed. A closed bifurcation line is referred to as a limit cycle.

In the present study, PIV measurements are carried out in a channel with periodic ribs on one wall. The emphasis of this study is to investigate the flow patterns in the vicinity of a rib. Topology-based visualization is also applied to examine the properties of the separation bubble upstream of the rib. The organization of this paper is as follows. Section 2 describes the experimental setup and measurement technique. We present and discuss results in Section 3 and draw conclusions in Section 4.

Email address: lei.wang@energy.lth.se (Lei Wang)

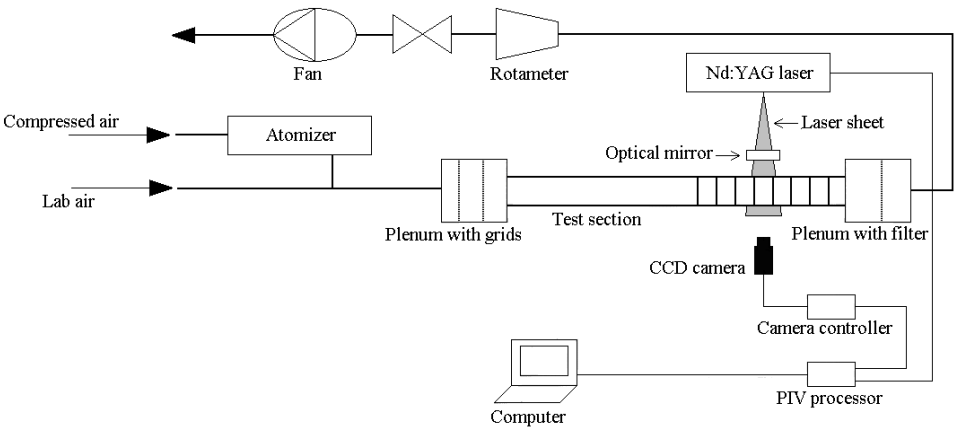

Figure 1: Sketch of experimental setup.

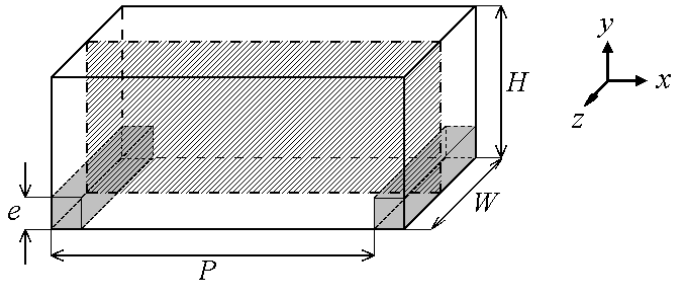

Figure 2: Rib configuration on one wall.

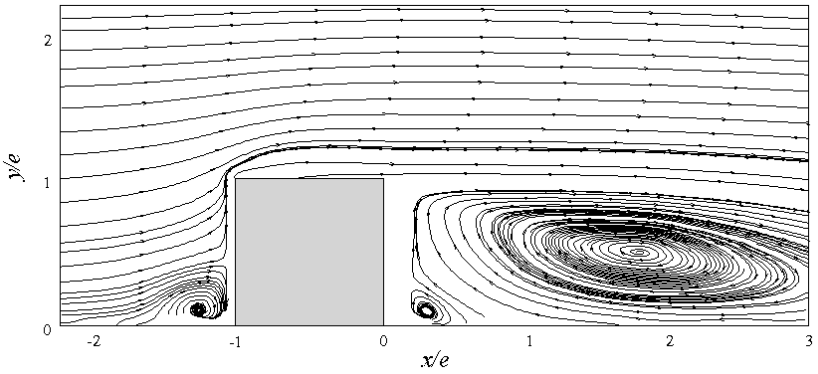

Figure 3: Side view of mean streamlines in the mid-span plane.

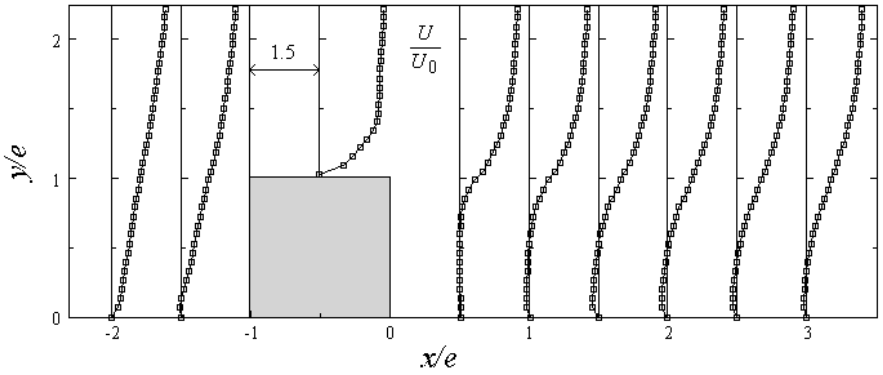

(a) U/U_0

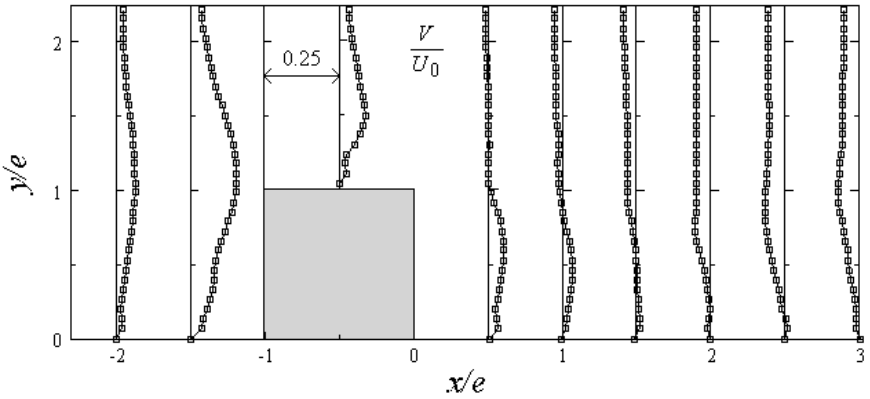

(b) V/U_0

Figure 4: Profiles of mean velocity normalized by the reference velocity U_0.

2. Experimental Procedures

The experimental setup is sketched in Fig. 1. Air with ambient temperature is sucked into the channel by a fan. The test section consists of a 1500 mm long channel with a cross section of 50 mm × 50 mm. The first half of the channel is smooth, and the second half of the channel is roughened with ribs. Only one wall is fitted with periodic transverse ribs. The height of the ribs is 10 mm which obstructs the channel by 20% of its height. The rib pitch, defined as the distance from one leading edge to the next leading edge, is 10 rib heights, as illustrated in Fig. 2. The inter-rib spacing is set such that the reattachment is allowed to take place on the portion between consecutive ribs. The rib height is represented by e, the rib pitch by P, and the channel height is denoted by H. The Cartesian coordinates x, y, z are defined in such a way that the x-axis is in the streamwise direction, the y-axis is the wall-normal direction, and z-axis is the spanwise direction. The measurements are made in the mid-span plane which is indicated in Fig. 2. The time-mean components of the velocity in the x- and y-directions are denoted by U and V, respectively, and the corresponding fluctuating components are denoted by u' and v'. The Reynolds number is 22000 based on the bulk-mean velocity $U_0 = 6.7$ m/s and the channel height H. In the present study, the flow around the seventh rib is investigated. This position is located at $x/D_h = 28$, where x is the distance of the seventh rib from the inlet, and D_h is the hydraulic diameter of the channel. According to Leonardi et al. [3], the roughness elements are virtually isolated as the cavity width to roughness height ratio is greater than 7 (or the pitch ratio is greater than 8). Throughout this paper, reference quantities for length and velocity are e and U_0, respectively.

A commercially available PIV system developed by Dantec Dynamics is used in the present investigation. An oil-based aerosol is generated by a TSI 9306 six-jet atomizer. In order to get a homogeneous distribution of seeding particles, a plenum with two grids is connected to the channel inlet. The mean particle diameter is about 1 μm and the concentration is regulated by the compressed air pressure and the number of Laskin nozzles. A Quantel Q-switched Nd:YAG laser provides pulsed illuminations with a wavelength of 532 nm. The duration of each pulse is 10 ns, and the maximum output energy is 120 mJ. The light-sheet thickness in the test section is kept at 0.8 mm. A digital camera containing a CCD chip with 1280×1024 pixels and a Nikon AF Micro 60f/2.8D lens with an optical filter are used to record the particle images. The size of the interrogation window is 32×32 pixels with 50% overlapping. This gives rise to the spatial resolution $\Delta/e = 0.067$ (Δ is the spacing between vectors). The time interval between laser pulses is set such that the particles move at most 8 pixels between the pair of images. In the present study, the time interval is 10 μs which gives the optimum measurement of the velocity. Within each window, the number of seeding particles is greater than 5 and the particle image size projected onto the CCD sensor is approximately 3 pixels. FlowMap software is used for the data processing. FFT-based cross-correlation in conjunction with a two-dimensional Gaussian fit is applied to find the correlation peak position. When the instantaneous velocity field is calculated, a peak-height validation and a moving-average validation are applied to the raw maps to detect and replace the 'outliers' by vectors estimated from surrounding values. To minimise the noise, a top-hat filter with uniform weighting is then implemented. The averaging area of the filter is 3×3 pixels. Assuming that the measured particle displacement is accurate to 0.1 pixels, the error is less than 2% for the displacement of 8 pixels. An ensemble of 1000 instantaneous velocity samples is generated with an acquisition rate of 4 Hz. It is found that the turbulent shear stresses converge well as the number of samples is greater than 700 (deviation is less than 3%). Another error affecting the Reynolds shear stress is the spatial resolution of PIV. For grid-generated turbulence, Lavoie et al. [10] found that the third-order structure function is more sensitive to PIV spatial resolution than the second-order one, but no ways for correcting the values were proposed. In the present experiment, the uncertainty for the shear stress is estimated to be about 10%, which takes into account of the number of samples and PIV spatial resolution.

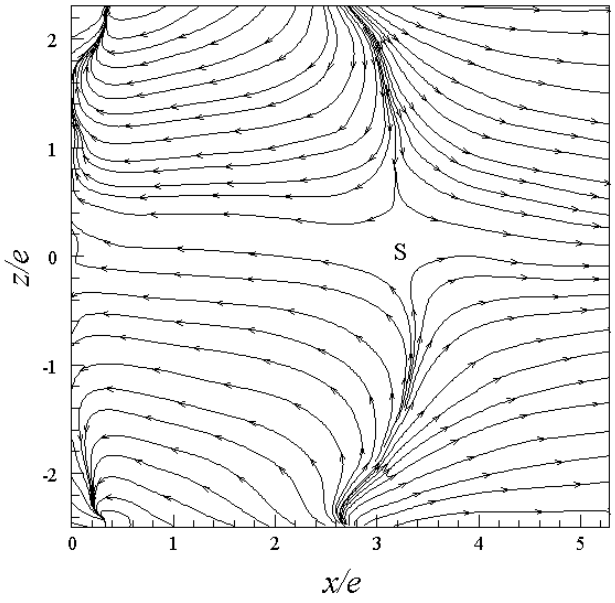

Figure 5: Top view of mean streamlines just above the wall. S denotes the saddle point.

3. Results

3.1. Overview of the flow

Prior to presenting detailed flow patterns in the vicinity of the rib, it is helpful to display some global flow features. Figure 3 shows the mean streamlines past the rib in the mid-span plane, where the origin is placed at the leeward corner of the rib. The most striking feature is the formation of a large recirculation bubble downstream of the rib. A secondary bubble is perceived in the leeward corner as the reverse flow approaches the vertical surface. Upstream of the rib, another separation bubble occurs as a result of the strong adverse pressure gradient. Figure 4 shows the mean velocity components at different streamwise

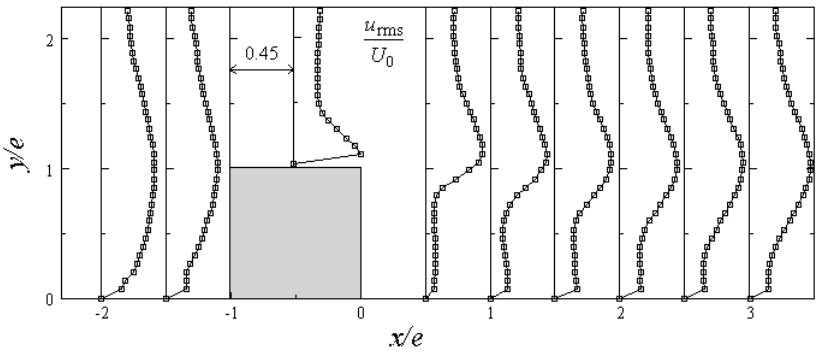

(a) u_{rms}/U_0

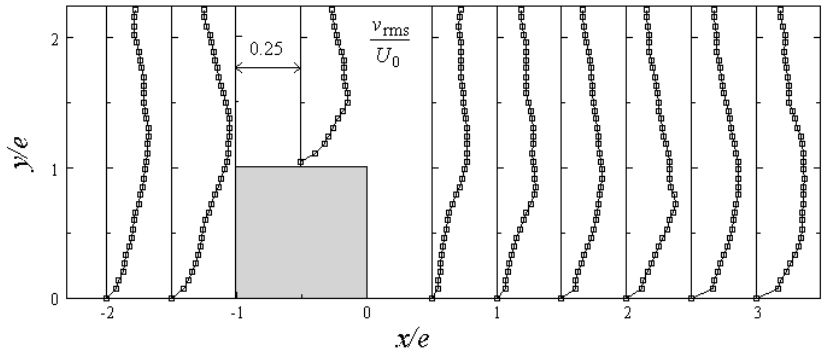

(b) v_{rms}/U_0

Figure 6: Profiles of normalized rms values.

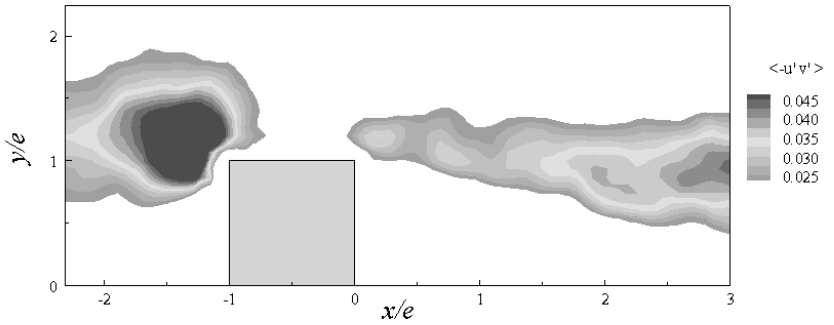

Figure 7: Contours of Reynolds shear stresses, the quantities are normalized by U_0^2.

locations in the mid-span plane. In Fig. 4a, the reverse flow coupled with the inflectional profiles is clearly demonstrated in the region downstream of the rib. Above the top of the rib, there is an intense shear layer and local acceleration. In Fig. 4b, the maximum outward velocity components are found ahead of the rib. Downstream of the rib ($x/e > 1$), the negative values of $\langle V \rangle$ suggest that the fluid is entrained from the central part of the flow to the wall as the separated shear layer curves inward. Figure 5 plots the mean streamlines downstream of the rib in the $x - z$ plane just above the wall. It should be mentioned that the exact wall-unit value of this plane is difficult to estimate because the laser sheet itself is 0.8 mm in thickness. In this figure, the spanwise reverse flow in conjunction with a curved reattachment line is clearly discerned. At the reattachment line, the shear layer bifurcates deflecting a fraction of fluid upstream and shedding remaining portion downstream. The reattachment point in the centerline exhibits the characteristics of a classical saddle point. Turbulence intensities in the streamwise and wall-normal directions are shown in Fig. 6. Downstream of the rib ($x/e > 0$), Fig. 6a shows that the position where u_{rms} attains a maximum value is around $y/e = 1.1$. This position can be interpreted as the center of the shear layer because it coincides with the inflectional point in the vertical distribution of U, as shown in Fig. 4. A large value of u_{rms} is found at the rib top, which is well in line with the simulated results by Cui et al. [11]. In Fig. 6b, the largest value of v_{rms} is found just ahead of the rib. Figure 7 displays the contours of the Reynolds shear stress. In this figure, only the quantities greater than $0.5\langle -u'v' \rangle_{max}$ are demonstrated in order to highlight the region with large Reynolds shear stresses. It is clear that the maximum Reynolds shear stresses occur at the leading edge of the rib, which is in good agreement with Cui et al. [11]. In the separated shear layer, the general trend is that the Reynolds shear stresses increase gradually with increasing distance from the rib.

3.2. Separated Shear Flow

In this section, consideration is given to the separated shear layer downstream of the rib. The plane $y/e = 1.1$ is taken to represent the shear layer. The first results to be discussed is the velocity probability density function (PDF) measured over a series of spatial positions in this plane behind the rib at $0 < x/e < 3$. Fluctuating velocity components are used to compute the PDF. The most remarkable features are the bimodal nature for u' and the sharp distribution for v'. Figure 8 shows such a PDF distribution at a representative position A ($x/e = 1.1$, $y/e = 1.1$). The bimodal feature indicates that the flow has two distinct modes corresponding to the peaks. Further inspection of the PDF distribution shows that the bimodal pattern exists in the whole separated shear layer between $y/e = 0.8$ and $y/e = 1.3$ behind the rib. The bimodal feature indicates that the flow contains periodicity, which is likely caused by the flapping motions of the shear layer sweeping over the measurement domain. The PDF distribution on the top of the rib at the plane $y/e = 1.1$ is also inspected. It is found that the bimodal feature continues to exist over the rear portion at $-0.5 < x/e < 0$, but it disappears over the front portion at $-1 < x/e < -0.5$. Further

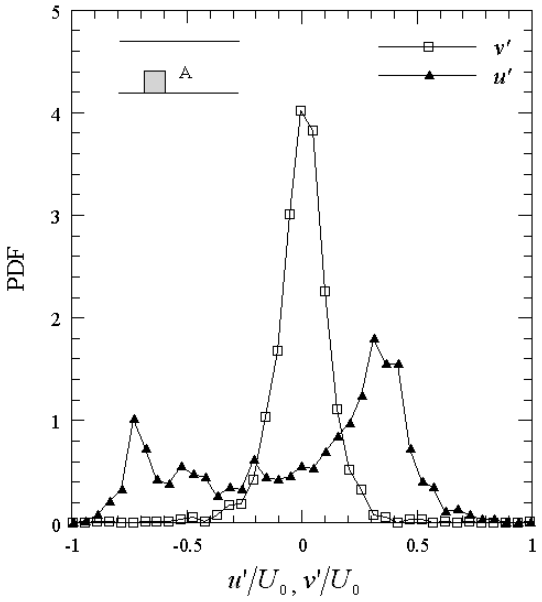

Figure 8: PDF distribution at a representative point A ($x/e = 1.1$, $y/e = 1.1$) in the separated shear layer.

away from the top of the rib ($y/e > 1.3$), there are no apparent bimodal distributions detected.

Another fundamental test is to compute the two-point correlation coefficients, which give an indication of how coherent the flow structure is over a certain distance. The correlation coefficient is defined as (with no implied summation)

$$R_{u_i u_j} = \frac{\langle u_i'(x_l) u_j'(x_k) \rangle}{\sqrt{\langle u_i'^2(x_l) \rangle \langle u_j'^2(x_k) \rangle}} \tag{1}$$

where $u_i'(x_l)$ and $u_j'(x_k)$ are two instantaneous velocity fluctuations. In this paper, we only consider the autocorrelation coefficient of the u' and v', denoted by R_{uu} and R_{vv}. Figures 9a and 9b show the contours of R_{uu} and R_{vv} in the mid-span plane. The point A ($x/e = 1.1$, $y/e = 1.1$) is selected as the reference location. In order to highlight the strongly correlated events, the quantities below the value 0.3 are disregarded. In Fig. 9a, the elongated contour of R_{uu} is nearly aligned in the x-direction, while the contour of R_{vv} is aligned in the y-direction. The y-alignment of R_{vv} was also noticed by previous studies in turbulent channel flow [12] and turbulent boundary layer flow over smooth and rough surface [13]. Further inspection of Fig. 9 shows that the spatial extent of R_{uu} is considerably greater than that of R_{vv}. This may be attributed to the large scale flapping motion of the separated shear layer.

3.3. Flow at the leading edge of the rib

As stated above, the maximum Reynolds shear stress occurs at the leading edge of the rib. One of the questions that remained unanswered is what kind of flow motions give rise to the Reynolds shear stress occurring in this region. To answer this question, we first investigate the probability density function distribution of the values. Figure 10 shows such a PDF

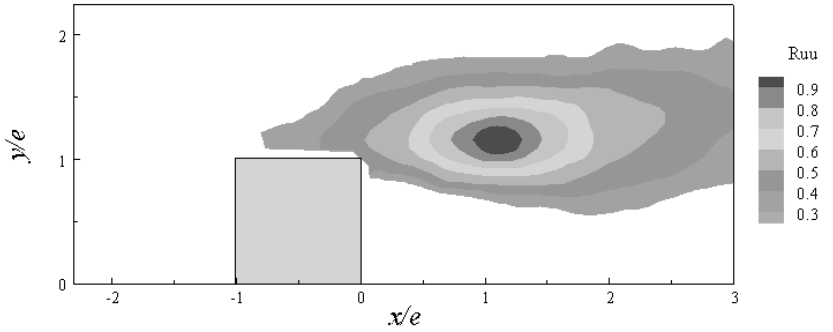

(a) R_{uu}

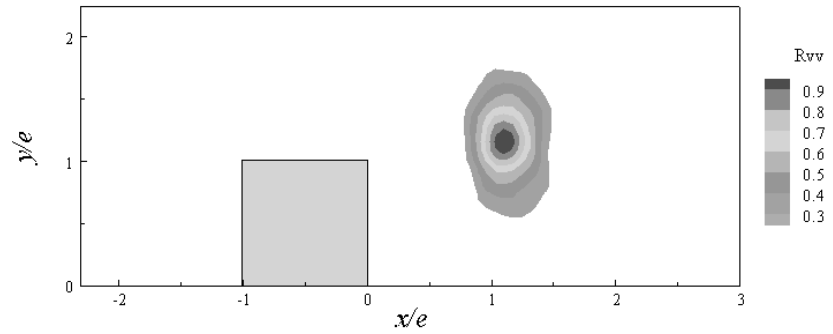

(b) R_{vv}

Figure 9: Contours of two-point correlation coefficients centered at point *A*.

profile at a representative point B ($x/e = -1.5, y/e = 1.1$). This point is located within the contour of the largest Reynolds shear stresses shown in Fig. 7. In this figure, the $-u'v'$ is normalized by its time-mean value $\langle -u'v' \rangle$. The PDF profile shows a sharp, skewed distribution with a long tail on the positive side. This means that the $-u'v'$ is most often a small value but it bursts occasionally. In other words, the $-u'v'$ is highly intermittent. To investigate the behaviour of $-u'v'$ further, we perform a quadrant analysis at point B. Quadrant analysis has been used in flat plate boundary layer flows by several investigators (for instance, Willmarth and Lu [14]; Bogard and Tiederman [15]) for predicting the types of turbulent motion and the scales contributing to these motions. The turbulent motions which make positive contribution to the Reynolds stress are identified as *ejection* ($u' < 0, v' > 0$) and *sweep* ($u' > 0, v' < 0$). The magnitude of contributing turbulent motions can be represented by the value of $-u'v'$ which is equal to or greater than a given threshold, or, $-u'v' \geq H \times \langle -u'v' \rangle$. Figure 11 presents the frequency of occurence of ejection and sweep events as a function of H. As $H = 1$, the number of ejections is roughly equal to the number of sweeps. With increasing value of H, the number of sweeps drops steeply. As $H > 5$, it is found that the ejections are the dominant events in the mechanism maintaining the Reynolds shear stress.

Figure 12 shows a typical PIV snapshot in which significant Reynolds shear stresses are produced at the leading edge of the rib. A pronounced feature is that the fluid is shed towards the main flow. The magnitude of the normal velocity is so large that

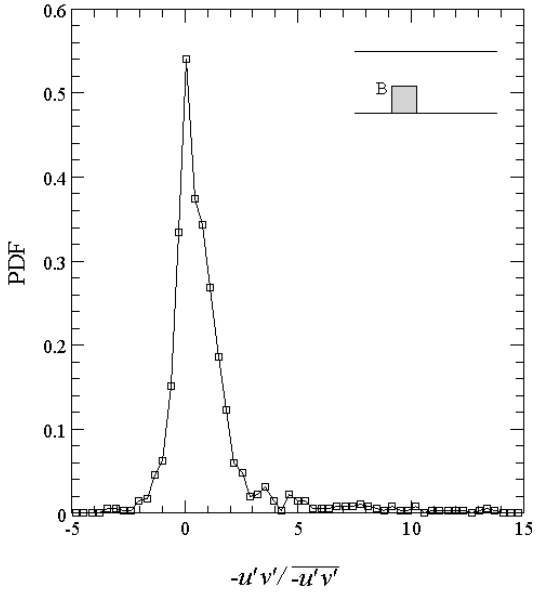

Figure 10: PDF of $-u'v'$ at a representative point B ($x/e = -1.5, y/e = 1.1$) at the leading edge of the rib.

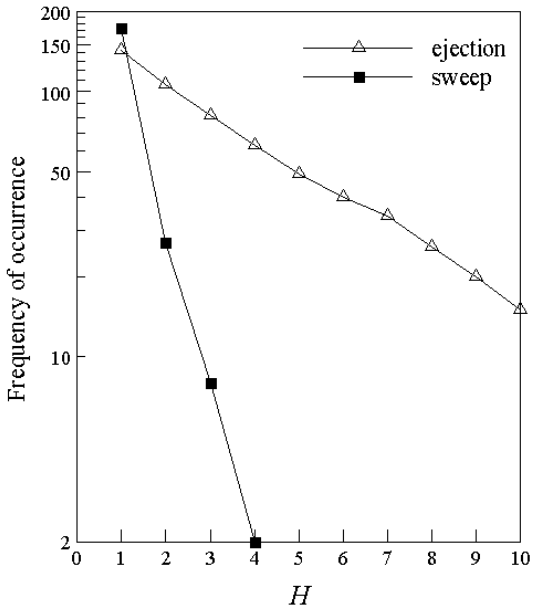

Figure 11: Frequency of occurence of $-u'v'$ as a function of the threshold H.

it is comparable to the reference velocity U_0. When the rapid upward motion encounters the incident main stream from the left, an inclined shear layer is observed. Despite the increased turbulent stresses at the leading edge of the rib, the upward motion is of practical significance in the cooling techniques since the hot fluid near the surface is shed towards the main flow.

3.4. Topology of the upstream separation bubble

Topology-based visualization of two-dimensional vector fields offers insight into the structure of flow [9]. In order to capture the essential topological structure of the separation bubble upstream of the rib, two methods are applied in this section to improve the quality of the velocity data. First, we increase the spatial resolution of PIV. Basically, the spacing between vectors in this section is 0.53 mm ($\Delta/e = 0.053$) and the investigated domain is upstream of the rib which contains 79×29 vectors. Figure 13 shows an instantaneous picture by PIV measurement. For the sake of convenience, the origin is placed at the windward corner of the rib. Apart from a primary separation bubble upstream of the rib, there is an additional separation bubble on the top of the rib. At the leading edge of the rib, a distinct upward shedding motion is also recognized. Furthermore, we use the proper orthogonal decomposition (POD) filter to smooth out random variations occurring in the flow. In contrast to the top-hat filter, the POD filter is inhomogeneous in one or more directions, which gives optimal results in the wall-bounded flow [16]. In POD, the velocity is expanded as a linear superposition of the mutually orthogonal eigenfunctions, in which the most energetic components are extracted. In a first approximation, the velocity can be represented by a low-order reconstruction which effectively removes the fine-scale, random variations from the total velocity field. In this study, the number of modes for reconstruction is 100 which contain 92.6% of the turbulent kinetic energy. For more details of POD, the reader is referred to Berkooz et al. [17]. Figure 14 gives the POD-filtered velocity field based on the PIV snapshot in Fig. 13. Generally speaking, the main flow structures in the vicinity of the rib remain unchanged but the separation bubble on the top of the rib looks more regular. In the following, the POD-filtered velocity data are used to compute the streamlines.

Figure 15 shows the close-up view of the mean streamlines associated with the separation bubble. It is clear that the streamlines within the bubble spiral into a focus instead of rotating about a center. This implies that the mean flow is not exactly two-dimensional even at the mid-span plane. In order to quantify how much the flow in the symmetry plane deviates from the idealized two-dimensional flow, the value of $\partial W/\partial z$ is calculated based on the continuity equation. Figure 15 presents the $\partial W/\partial z$ values which are normalized by $1000e/U_0$. Outside the separation bubble, as expected, the flow is essentially two-dimensional due to the vanishing value of $\partial W/\partial z$. However, the large deviation of $\partial W/\partial z$ from zero within the separation bubble indicates the separation bubble is really three-dimensional. This result shows that the topology gives an indication of whether the flow is two-dimensional or not.

Figure 16 demonstrates the instantaneous flow in the separation bubble, in which various critical points are illustrated. It should be noted that all the bubbles rotate in a clockwise sense. Figure 16a illustrates an attracting (or stable) focus towards which the neighboring streamlines converge in a spiral manner. However, in Fig. 16b, the striking feature is a repelling (or unstable) focus from which all the neighboring streamlines depart in a spiral manner. Accompanying the unstable focus is a bifurcation line (denoted by G) towards which other streamlines converge asymptotically. It should be mentioned that unstable foci are much outnumbered by the stable ones in our experiment. In Fig. 16c and d, there are two different types of critical points involved: two stable foci and in between a saddle point. Further examination of Fig. 16 shows that the vortices change in number during the experiment. In Fig. 16a and b, there is only a single separation bubble, while in Fig. 16c and d, a primary separation bubble together with a secondary vortex is observed. However, it should be noted that the two vortex flow patterns are rarely observed in our experiments. Since a focus cannot take place in two-dimensional flows, Fig. 16 reveals that the separation bubble upstream of the rib is intrinsically three-dimensional.

In addition to the critical points, it is also found that the limit cycles characterize the separation bubble. Figures 17a-e displays close-up views of various limit cycles. In general, the limit cycle is elliptic with a principal axis. It should be noted that the streamlines inside the limit cycle are not drawn in Figs. 17a-d. This is due to the weak convergence of streamlines, i.e. it takes a large number of rotations to approach the limit cycle. If the streamlines inside the limit cycle were displayed otherwise, it would be hard to identify a closed orbit. In Fig. 17e, the convergence is relatively fast and a distinct limit cycle is observed. Further inspection of Fig. 17 shows that the size of the limit cycle varies from time to time, which suggests that the vortex tube undergoes axial stretching or compression.

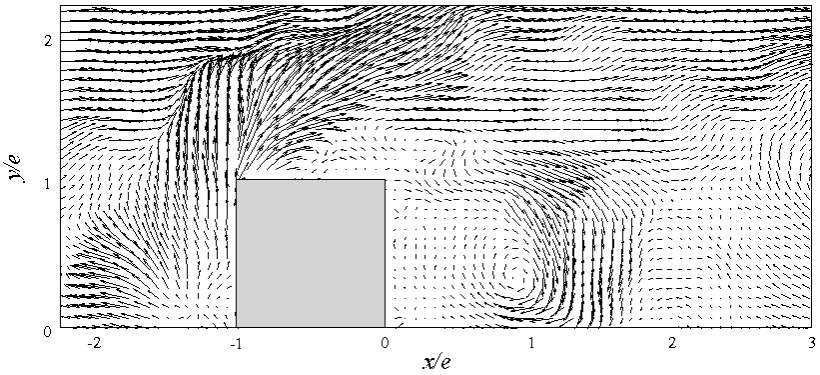

Figure 12: A PIV snapshot which produces significant Reynolds shear stresses at the leading edge of the rib.

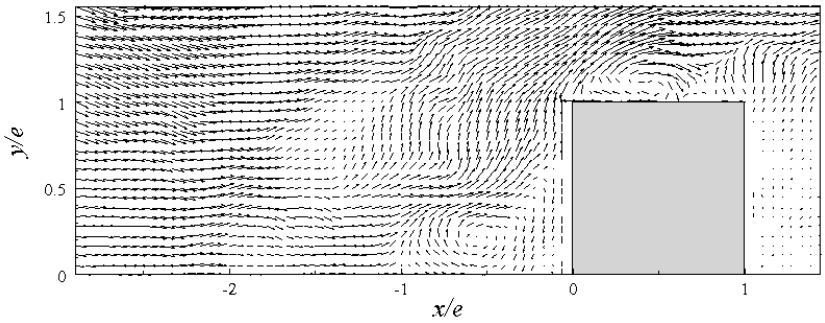

Figure 13: Instantaneous flow obtained by PIV.

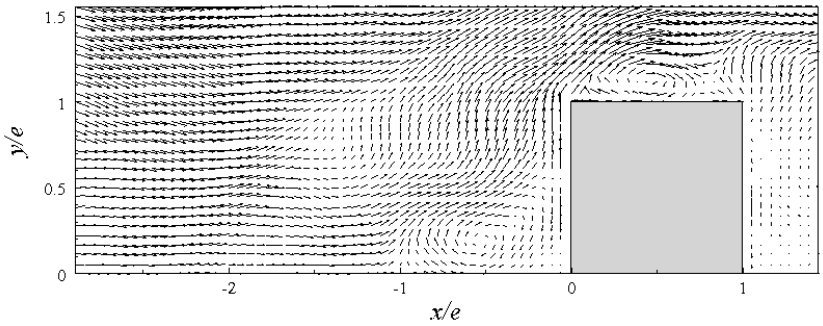

Figure 14: POD-filtered velocity field.

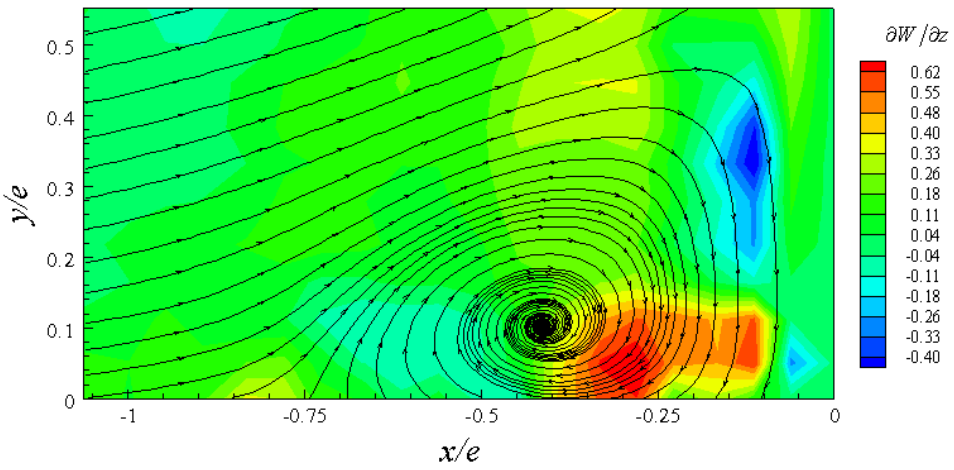

Figure 15: Close-up view of the mean streamlines of the separation bubble.

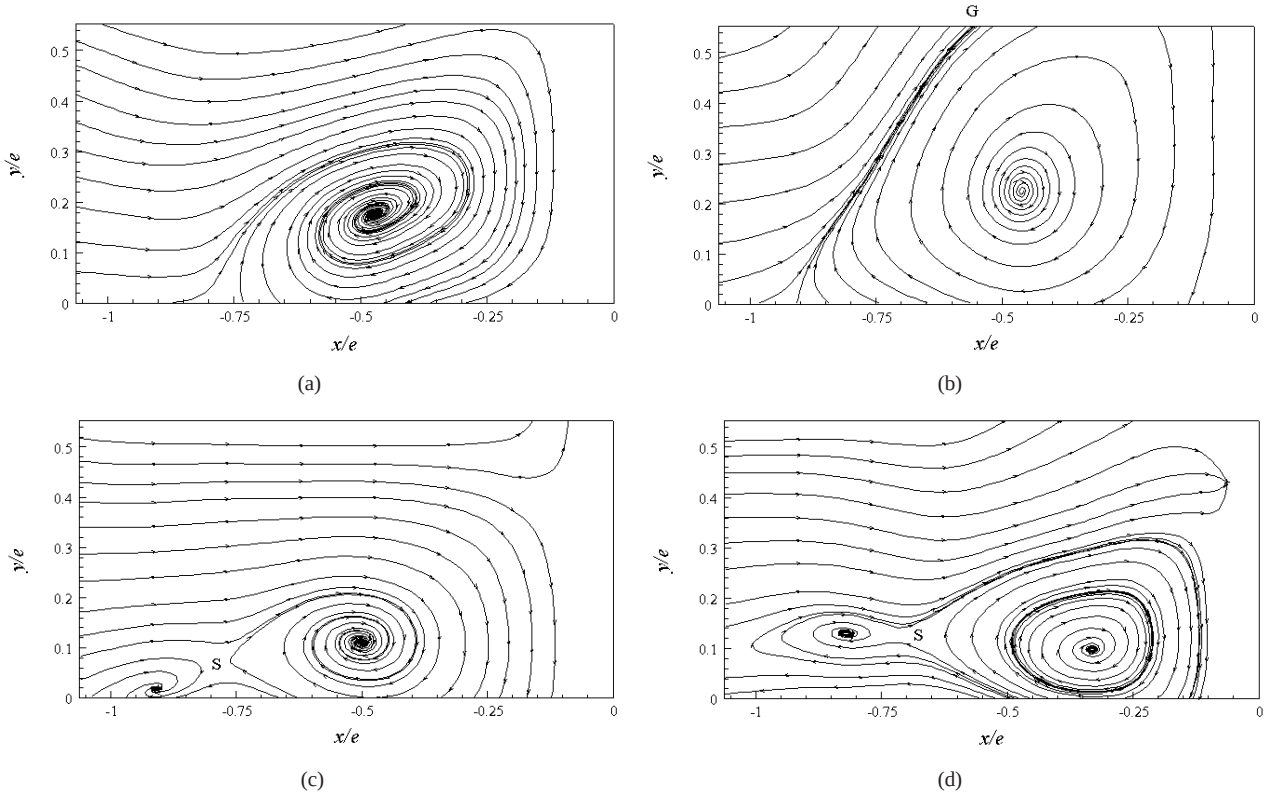

Figure 16: Various critical points in the separation bubble.

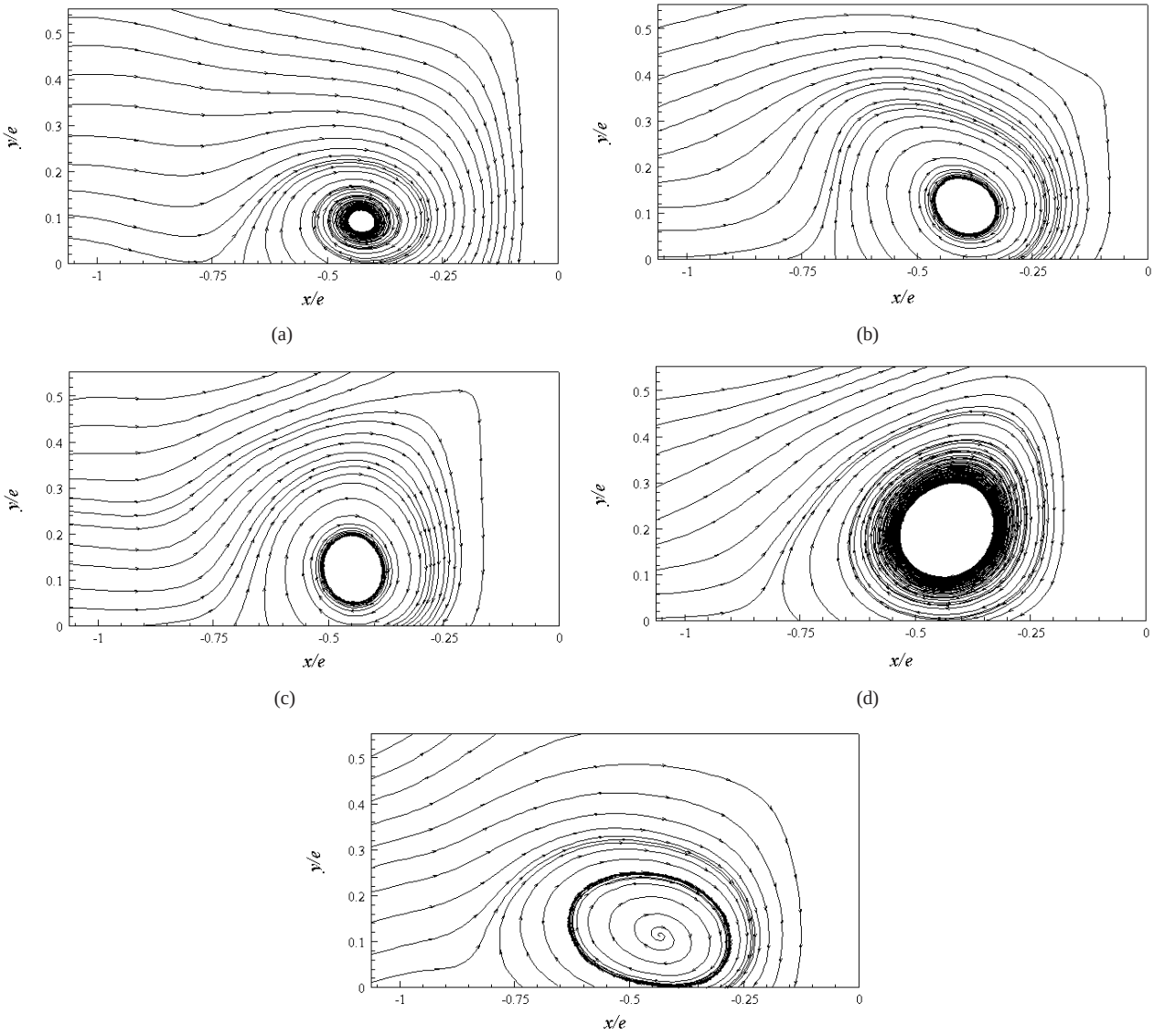

Figure 17: Limit cycles in the separation bubble.

Critical points and limit cycles shown in Figs. 16 and 17 can give us more information on the properties of the separation bubble. It is known that the Burger's single-cell vortex is a characteristic of an attracting focus [18] and the Sullivan's two-cell vortex is consistent with a limit cycle [19]. Here the two-cell vortex means that the flow does not simply spiral towards the central axis and out along it as the single-cell vortex does, but has a region of reverse flow near the central axis. Therefore, the appearance of various critical points and limit cycles in this study signifies that the separation bubble changes essentially in structure during the course of time.

4. Conclusions

In this study, PIV measurements are performed in a channel with periodic ribs on one wall. The ribs obstruct the channel by 20% of its height and are arranged 10 rib heights apart. The Reynolds number is 22000 based on the bulk-mean velocity and channel height. The emphasis of this study is to investigate the flow structures in the vicinity of a rib. An important feature is the bimodal PDF distribution of u' in the separated shear layer downstream of the rib. This is probably caused by the large scale flapping motion of the separated shear layer. The maximum Reynolds shear stresses occur at the leading edge of the rib. Based on the quadrant analysis, it is found that the ejection motions make a dominant contribution to the Reynolds shear stress in this region. Upstream of the rib, salient critical points and limit cycles are extracted to sketch the topological structures of the separation bubble. The knowledge of their properties gives clues to the physical processes occurring in the flow.

Acknowledgments

The current research is financially supported by the Swedish Research Council (VR) and the Swedish National Energy Agency (STEM).

References

[1] R.L. Webb, Principles of Enhanced Heat Transfer, John Wiley & Sons Inc., New York, 1994.
[2] P. Bradshaw, F.Y.F. Wong, The reattachment and relaxation of a turbulent shear layer, J. Fluid Mech. 52 (1972) 113-135.
[3] S. Leonardi, P. Orlandi, R.J. Smalley, L. Djenidi, R.A. Antonia, Direct numerical simulation of turbulent channel with transverse square bars on one wall, J. Fluid Mech. 491 (2003) 229-238.
[4] G. Rau, M. Cakan, D. Moeller, T. Arts, The effect of periodic ribs on the local aerodynamic and heat transfer performance of a straight cooling channel, ASME J. Turbomachinery 120 (1998) 368-375.
[5] T. Mullin, S.R. Martin, Intermittent phenomena in the flow over a rib roughened surface, ASME J. Fluids Eng. 113 (1991) 206-209.
[6] L. Wang, J. Hejcik, B. Sundn, PIV measurements of separated flow in a square channel with streamwise periodic ribs on one wall, ASME J. Fluids Eng. 129 (2007) 834-841.
[7] R. Martinuzzi, C. Tropea, The flow around surface-mounted, prismatic obstacles placed in fully developed channel flow, ASME J. Fluids Eng. 115 (1993) 85-92.
[8] J.H. Chou, S.Y. Chao, Branching of horseshoe vortex around surface-mounted rectangular cylinders, Exp. Fluids 28 (2000) 394-402.
[9] A.E. Perry, M.S. Chong, A description of eddying motions and flow patterns using critical-point concepts, Ann. Rev. Fluid Mech., 19 (1987), 125-155.
[10] P. Lavoie, G. Avallone, F. De Gregorio, G.P. Romano, R.A. Antonia, Spatial resolution of PIV for the measurement of turbulence, Exp. Fluids 43 (2007) 39-51.
[11] J. Cui, V.C. Patel, C.L. Lin, Large-eddy simulation of turbulent flow in a channel with rib roughness, Int. J. Heat Fluid Flow 24 (2003) 372-388.
[12] J. Kim, F. Hussain, Propagation velocity and space-time correlation of perturbations in turbulent channel flow, NASA TM 103932 (1992).
[13] P.Å. Krogstad, R.A. Antonia, Structure of turbulent boundary layer on smooth and rough walls, J. Fluid Mech. 277 (1994) 1-21.
[14] W.W. Willmarth, S.S. Lu, Structure of the Reynolds stress near the wall, J. Fluid Mech. 55 (1972) 65-72.
[15] D.G. Bogard, W.G. Tiederman, Characteristics of ejections in turbulent channel flow, J. Fluid Mech. 179 (1987) 1-19.
[16] R.J. Adrian, K.T. Christensen, Z.C. Liu, Analysis and interpretation of instantaneous turbulent velocity fields, Exp. Fluids 29 (2000) 275-290.
[17] G. Berkooz, P. Holmes, J.L. Lumley, The proper orthogonal decomposition in the analysis of turbulent flows, Ann. Rev. Fluid Mech. 25 (1993) 539-575.
[18] J.M. Burgers, A mathematical model illustrating the theory of turbulence, Adv. in Applied Mechanics 1 (1948) 171-199.
[19] R.D. Sullivan, A two-cell solution of the Navier-Stokes equations, J. Aero. Sci. 26 (1959) 767-768.